THE JOURNAL OF PHYSICAL CHEMISTRY B
A JOURNAL OF THE AMERICAN CHEMICAL SOCIETY

pubs.acs.org/JPCB

Article

Rethinking Vibrational Stark Spectroscopy: Peak Shifts, Line Widths, and the Role of Non-Stark Solvent Coupling

Published as part of The Journal of Physical Chemistry virtual special issue "Steven G. Boxer Festschrift".

Sebastian M. Fica-Contreras, Aaron P. Charnay, Junkun Pan, and Michael D. Fayer*

Cite This: *J. Phys. Chem. B* 2023, 127, 717−731

Read Online

ACCESS | Metrics & More | Article Recommendations | Supporting Information

ABSTRACT: A vibration's transition frequency is partly determined by the first-order Stark effect, which accounts for the electric field experienced by the mode. Using ultrafast infrared pump−probe and FT-IR spectroscopies, we characterized both the 0 → 1 and 1 → 2 vibrational transitions' field-dependent peak positions and line widths of the CN stretching mode of benzonitrile (BZN) and phenyl selenocyanate (PhSeCN) in ten solvents. We present a theoretical model that decomposes the observed line width into a field-dependent Stark contribution and a field-independent non-Stark solvent coupling contribution (NSC). The model demonstrates that the field-dependent peak position is independent of the line width, even when the NSC dominates the latter. Experiments show that when the Stark tuning rate is large compared to the NSC (PhSeCN), the line width has a field dependence, albeit with major NSC-induced excursions from linearity. When the Stark tuning rate is small relative to the NSC (BZN), the line width is field-independent. BZN's line widths are substantially larger for the 1 → 2 transition, indicating a 1 → 2 transition enhancement of the NSC. Additionally, we examine, theoretically and experimentally, the difference in the 0 → 1 and 1 → 2 transitions' Stark tuning rates. Second-order perturbation theory combined with density functional theory explain the difference and show that the 1 → 2 transition's Stark tuning rate is ∼10% larger. The Stark tuning rate of PhSeCN is larger than BZN's for both transitions, consistent with the theoretical calculations. This study provides new insights into vibrational line shape components and a more general understanding of the vibrational response to external electric fields.

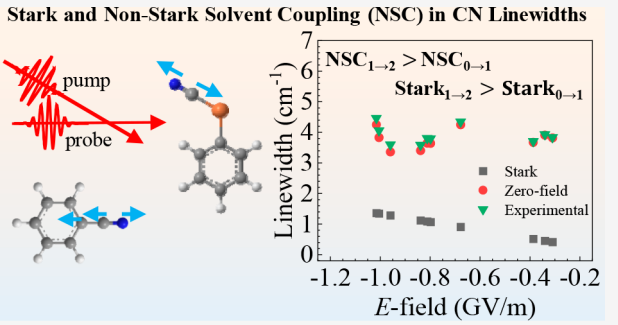

I. INTRODUCTION

Molecular vibrational modes can be used to investigate the electric fields impinging on a molecule by observing vibrational frequency shifts that arise from the vibrational Stark effect (VSE).[1−6] These vibrational frequency shifts are useful for distinguishing between different chemical environments, as well as for studying the influence that electric fields have on chemical and biological processes.[7−11] The VSE has been used to study electric fields in enzymes,[4,12−15] polymers,[16] liquids,[17−20] and interfaces.[21−25]

The vibrational Stark effect is composed of a first-order component that results from the molecule's permanent dipole moment, and a much weaker second-order component that arises from its polarizability.[26] For a first-order Stark effect to exist, the molecule must have a nonzero permanent dipole moment that is not orthogonal to the vibrational mode of interest.[1] When a first-order Stark effect occurs, the second-order contribution is generally negligible and usually not considered.[26] The experiments and theory presented below study nitriles, which have well-documented, large first-order Stark effect contributions,[1,26,27] and elucidate new aspects of the VSE. While we only focus on the study of nitriles, our results are general. Nitriles are useful as vibrational probes because they typically display a single vibrational mode; they have moderately large transition dipoles, which yield reasonable signal amplitudes for linear and nonlinear infrared spectroscopy experiments,[28] and have relatively large solvatochromic shifts that permit the study of environment specific dynamics.[27]

While VSE research has focused on understanding electric field-dependent vibrational frequency shifts, the effect that these have on the line widths, and other possible contributions, has not generally been considered. Moreover, VSE has been studied and used in a variety of applications with linear absorption spectroscopy,[1,28,29] where the relevant energy levels are the vibrational ground state, $|0\rangle$, and first vibrational

Received: August 24, 2022
Revised: December 6, 2022
Published: January 11, 2023

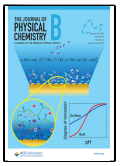

excited state, $|1\rangle$. As a result, experimental and theoretical research focuses on the study of the VSE for the $0 \rightarrow 1$ vibrational transition, but the nature of the Stark effect (frequency shifts and line width changes) for higher-energy transitions has not been investigated.

It is the purpose of this paper to present aspects of the VSE that provide an increased understanding of the origin of vibrational frequency shifts and line widths. Specifically, we explore the origin of the changes in line widths of two similar molecular structures, classify intermolecular interactions into Stark and non-Stark components, and quantify their relative contributions for ten solvents. Further, we study the differences in the manifestations of the VSE for the $0 \rightarrow 1$ and $1 \rightarrow 2$ transitions. While we only considered transitions up to the $|2\rangle$ level, the method presented here can be applied to higher lying transitions as well. Nonlinear infrared spectroscopy is well-suited for this study because IR pump−probe spectroscopy can simultaneously measure vibrational frequencies and line shapes for both $0 \rightarrow 1$ and $1 \rightarrow 2$ transitions.

The solvent-dependent line shapes of phenyl selenocyanate (PhSeCN) and benzonitrile (BZN) were decomposed into a VSE component and a field-free component referred to as the Stark and non-Stark solvent coupling contribution (NSC), respectively. The analysis shows that, in addition to a Stark contribution, the CN mode has a solvent-dependent vibrational frequency and line width contribution to the spectra from field-free solute/solvent intermolecular interactions. Whether the Stark contribution or the NSC dominates is dependent on the solvent, the molecule, and the transition. The NSC is important in determining the commonly observed nonlinearity of the field-dependent vibrational frequency shifts, and it is essential in understanding the observed solvent-dependent line widths of a vibrational transition. The NSC width is much broader in BZN than in PhSeCN, which combined with a smaller Stark tuning rate in BZN, results in the complete loss of an *E*-field-dependent line width. For PhSeCN, which has a significantly larger Stark tuning rate, the Stark contribution to the line width is observable in addition to the NSC to yield a linear *E*-field-dependent line width but with major deviations. Finally, this effect is more pronounced in the $1 \rightarrow 2$ transition of BZN than in its $0 \rightarrow 1$ transition.

Some evidence of an increase in the Stark tuning rate in the $1 \rightarrow 2$ transition was observed for BZN and PhSeCN. The coupling of the vibrational mode to solvent electric fields results from the difference in molecular dipole moment in the two states involved in the transition. The coupling strength is quantified as the dipole moment difference vector projected onto the bond axis of interest, i.e., for nitriles, the CN bond.[1] An analytical analysis based on second-order perturbation theory and density functional theory demonstrated that enhancement of the Stark tuning rate for the $1 \rightarrow 2$ transition should be expected in general, and that it should be more pronounced in BZN than in PhSeCN. However, the magnitude of this effect is too small to be accurately measured with experiments, and it can be overshadowed by the NSC component.

This study elucidates aspects of Stark spectroscopy that are important to the interpretation of the spectral changes observed in solvatochromic calibrations; it provides insights into the energy-level-dependent manifestation of the Stark effect, and it demonstrates that line shape changes are not determined by the first-order Stark effect alone.

This paper is organized as follows. We describe the first-order Stark effect in Section II. Section III contains the experimental, theoretical, and computational methods used in this study. In Section IV.A, we discuss the origin of a pump−probe signal and the canonical interpretation of its features, and in Section IV.B, experimental evidence of distinct behavior in the signal of BZN compared to that of PhSeCN is presented. The field-dependent CN vibrational frequencies and line widths of both molecules in the $0 \rightarrow 1$ and $1 \rightarrow 2$ transitions are presented and discussed in Section IV.C. In this section, we discuss deviations from linearity in the vibrational frequency shifts for high *E*-fields, observe an anomalously large and field-independent line width in BZN, and identify field-independent solute−solvent interactions as the physical root cause for these observations. In Section IV.D, a convolution model is used to decompose the vibrational frequencies and line widths into VSE and NSC components. We show that a linear field-dependent VSE cannot account for the experimental results, and that the NSC is necessary across all solvents. Additionally, we show that the NSC magnitude overwhelms the line width in BZN and that it increases for the $1 \rightarrow 2$ transition. Finally, in Section IV.E, density functional theory and second-order perturbation theory are used to show that the Stark tuning rate is greater for the $1 \rightarrow 2$ transition compared to the $0 \rightarrow 1$, but the effect is not large enough to account for the experimental observations listed above.

II. BRIEF DESCRIPTION OF THE FIRST-ORDER STARK EFFECT

For the hypothetical case of a molecule in a condensed phase system that is isolated from solvent electric fields, the vibrational mode of interest would have a frequency ω_0, the zero-field vibrational frequency. This frequency is not the gas phase frequency as there are intermolecular interactions with the solvent that are not due to the solvent's electric field, such as van der Waals and repulsion interactions.[30] While this concept has been explored in the past in the context of predicting $0 \rightarrow 1$ vibrational frequency shifts in H-bonding protein environments, where it was shown that a simple Coulombic interaction is not sufficient to describe experimental results,[30,31] no study that includes higher-energy transitions exists.

When the molecule is under the influence of an electric field, its electronic potential is changed.[2] The electric field interaction shifts the ground and first excited vibrational states by different extents and causes the transition frequency of the vibrational mode to shift linearly with the field magnitude as[21]

$$\omega = \Delta\vec{\mu}\cdot\vec{E} + \omega_0 \tag{1}$$

Here, $\Delta\vec{\mu}$ is the dipole moment difference vector in Debye (D) of the two states that give rise to the observed transition, and $\vec{E}$ is the electric field impinging on the molecule. The dipole moment difference vector, also known as the Stark tuning rate, determines the sensitivity of the vibrational mode to the electric field. It originates from the difference in projection magnitude of the molecule's dipole moment vector onto the bond axis of the mode under study for the two energy levels involved in the transition.[1]

The Onsager reaction field model is used to quantify the solvent's electric field magnitude.[1] In this model, the vibrational probe molecule occupies a spherical cavity with

https://doi.org/10.1021/acs.jpcb.2c06071
J. Phys. Chem. B 2023, 127, 717−731

an electric field magnitude equal to the average electric field generated by the solvent,[1] which is given by[32]

$$E = \frac{\vec{\mu}_0}{4\pi\varepsilon_0 a^3}\left(\frac{2(\varepsilon - 1)(n^2 + 2)}{3(2\varepsilon + n^2)}\right) \quad (2)$$

where a is the radius of the solvent cavity (related to the vibrational probe's molecular weight and density), $\vec{\mu}_0$ is the permanent molecular dipole moment in the ground state, ε_0 is the permittivity of free space, ε is the static dielectric constant of the solvent, and n is the refractive index of the probe molecule.

A determination of the Stark tuning rate is performed by measuring the absorption spectra of the vibrational mode in a series of non-hydrogen-bonding solvents of varying static dielectric constant. Equations 1 and 2 are then combined to relate the observed vibrational frequencies (peak frequencies) of the mode to the average electric field magnitude of the solvent. The slope of a linear regression (eq 1) of a plot of frequency vs field provides the Stark tuning rate of the vibrational mode.[1] The intercept at zero field is ω_0. In subsequent sections, we recreate this type of calibration for BZN and PhSeCN in 10 solvents and show that the simple relation described by eq 1 is not sufficient to replicate the experiments. Further, we decompose the vibrational frequency shifts as well as the line widths into Stark and NSC contributions.

III. EXPERIMENTAL PROCEDURES

III.A. Fourier Transform Infrared (FT-IR) Spectroscopy. PhSeCN and BZN probe molecules were dissolved in a series of non-hydrogen-bonding solvents of varying polarity at a concentration of 250 and 100 mM, respectively. Each solution was placed in a copper sample cell with two calcium fluoride (CaF_2) windows separated by a 250 μm Teflon spacer. The linear infrared absorption spectrum of the CN stretch of PhSeCN and BZN in each sample was collected using a resolution of 0.24 cm^{-1} (see Section S5). Background subtraction was performed by collecting the probe-free absorption spectrum of each solvent and subtracting it from the corresponding spectrum of the sample with the probe.

III.B. Excited State Spectrum. The spectrum of the transition between the $|1\rangle$ and $|2\rangle$ vibrational levels was collected using an ultrafast infrared spectrophotometer. The details of an analogous instrument have been published previously.[33,34] Briefly, a Ti:sapphire oscillator–seeded regenerative amplifier pumped an optical parametric amplifier to generate 4.6 μm pulses (30 μJ and 3 kHz repetition rate). The 4.6 μm pulses had a bandwidth of 100 cm^{-1} and were near transform-limited. The mid-IR was tuned to be resonant with the vibrational frequency of the CN stretch of the probe of interest.

The IR pulse was split into a strong pump pulse (~90% intensity) and a weak probe pulse (~5% intensity). The pump was passed through a germanium acousto-optic modulator (AOM), which was used to block the frequencies of light resonant with the nitrile stretch in every other pump pulse.[35] Pump and probe pulses overlapped in the sample, and their separation in arrival time was controlled with a mechanical delay stage. The probe pulse with parallel polarization relative to the pump was directed into a single-element mercury–cadmium-telluride (MCT) detector through a monochromator. The monochromator was scanned over a 60 cm^{-1} range in steps of 0.25 cm^{-1} to record the spectrum of the nonlinear signal. The pump–probe spectra were recorded with a single delay time close to zero, as the spectrum, not its time dependence, was of interest.

III.C. Density Functional Theory (DFT) Calculations. Geometry optimization of the PhSeCN and BZN structures was performed using Gaussian 09 with functional B3WP91 and basis set 6-311G (2df, p). This level of theory was used because it has been found to yield accurate vibrational energies, especially for seleno-organic compounds.[36,37] Geometry optimization was performed using a tight convergence criterion and a superfine integration grid. A subsequent vibrational frequency calculation was performed on both molecules using a Gaussian 09 built-in anharmonic correction function on the CN symmetric stretch normal mode.[38,39] It was confirmed that the level of theory used yields vibrational frequencies for the CN stretch fundamental that are only 3.4% higher than the experimental values for both PhSeCN and BZN (see Section S1).

A relaxed potential energy surface (PES) calculation was performed to stretch and compress both PhSeCN and BZN along the CN stretching normal mode over a range of ±0.2 Å from the equilibrium position in steps of 0.01 Å. The molecular dipole moment was computed at each step of the calculation to obtain a displacement-dependent molecular dipole curve. Using the Cartesian coordinates of the atoms at every optimized structure of the calculation, the projection of the permanent molecular dipole moment vector onto the CN bond axis was calculated to obtain a displacement-dependent permanent dipole moment projection curve. Finally, the Mulliken charges of all atoms were computed for every optimized geometry to obtain the flow of charge across the structures as a function of molecular displacement (see Section S7).

IV. RESULTS AND DISCUSSION

IV.A. Origin of the Pump–Probe Signal. Figure 1 shows a schematic representation of a pump–probe signal (right) and of the vibrational transition processes involved in generating it (left). The pump–probe signal is generated using two mid-infrared ultrashort laser pulses. The mathematical details of the

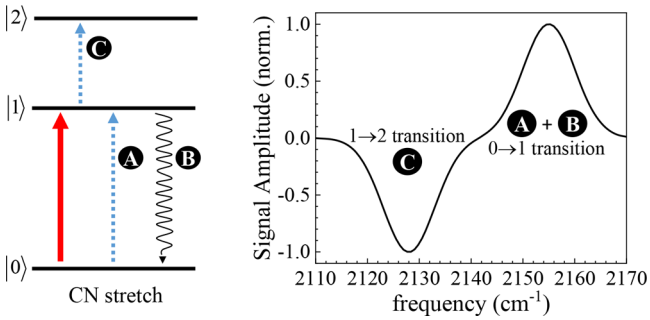

Figure 1. Schematic representation of a typical pump–probe signal and the transition processes involved in generating it. The signal is composed of one positive- and one negative-going feature, separated by the vibrational anharmonicity of the mode (see the text). The positive-going feature results from ground state bleaching (A) and stimulated emission (B), whereas the negative-going feature results from excited state absorption (C). Generally, the amplitude and width of the two features are expected to be the same, but experiments presented here show that this is not always correct.

https://doi.org/10.1021/acs.jpcb.2c06071
J. Phys. Chem. B 2023, 127, 717–731

origin of this signal are well-established.[40,41] Here, the origin of the signal is discussed qualitatively. The strong pump pulse (red solid arrow) excites an anisotropic distribution of molecules in the sample from the ground state, $|0\rangle$, to the first excited vibrational state, $|1\rangle$. As a result, the population in $|0\rangle$ is diminished, and the population in $|1\rangle$ is created. The probe pulse impinges on the sample at a later time, t, and experiences three different processes. The first process (A) is a decreased absorption as molecules excited by the pump no longer absorb light at the 0 → 1 frequency. Additionally, because the pump creates population in $|1\rangle$, the probe pulse also induces stimulated emission (B) from $|1\rangle$ to $|0\rangle$, which amplifies the probe intensity at ω_{01}. Both A and B processes contribute to increasing transmission through the sample and result in a net positive-going signal for the 0 → 1 transition (Figure 1, right panel). Additionally, upon arrival of the probe pulse, excited state absorption (C) occurs with molecules in $|1\rangle$ excited to $|2\rangle$. This process is a new absorption, and it occurs at the frequency of the vibrational transition from $|1\rangle$ to $|2\rangle$, ω_{12}. A new absorption decreases transmission, and it results in a negative-going feature, the 1 → 2 transition (Figure 1, right panel). The two transitions are separated in frequency by the anharmonicity of the vibrational mode. The intensity of the contribution of each process to the signal amplitude is determined by the transition dipole strength of the molecule. In the harmonic approximation, the transition dipole of the 1 → 2 transition is $\sqrt{2}$ larger than the 0 → 1 transition. Once the pump pulse has created population in the $|1\rangle$ state, the probe signal depends on the square of the transition dipole. There are two pathways for the 0 → 1 transition signal (A and B on the left side of Figure 1), but only one pathway for the 1 → 2 transition signal. However, the 1 → 2 transition signal is twice as big as a single 0 → 1 transition pathway. The net result is that the signals for the two transitions are identical in magnitude but opposite in sign as shown in the right panel of Figure 1. Since the two signals originate from the same subensemble of molecules selected by the pump pulse, in the simplest situation, the two line shapes for the 0 → 1 and 1 → 2 transitions would be identical. It will be shown in subsequent sections that the line shapes of the two transitions are not and should not be expected to be identical, and the physical origin of this effect is discussed. It is important to note that the 0 → 1 pump−probe spectrum is delay-time-independent and is identical to the 0 → 1 FT-IR spectrum.

IV.B. Line Shapes in Benzonitrile and Phenyl Selenocyanate. Figure 2A shows the pump−probe signal of the CN stretching mode of PhSeCN and BZN in dimethylformamide (DMF) fitted with Gaussian functions. A Gaussian functional form quantitatively reproduces the experimental data and demonstrates that the main broadening mechanism in these systems is inhomogeneous in nature. The center frequencies of the 0 → 1 and 1 → 2 transitions of PhSeCN are 2152.1 and 2126.1 cm^{-1}, respectively. For BZN, the 0 → 1 transition is centered at 2228.3 cm^{-1} and the 1 → 2 transition at 2203.6 cm^{-1}. These values are consistent with previous reports of the center frequencies of the CN stretch mode of both PhSeCN and BZN.[1,16] The observed anharmonicities, $\Delta\omega$, are 26.0 and 24.7 cm^{-1} for PhSeCN and BZN, respectively. While the signal from PhSeCN meets the description discussed in connection with Figure 1 (right side), with identical 0 → 1 and 1 → 2 transitions, the signal obtained from BZN does not. There is a substantial difference between the two transition line shapes in BZN. The full-width

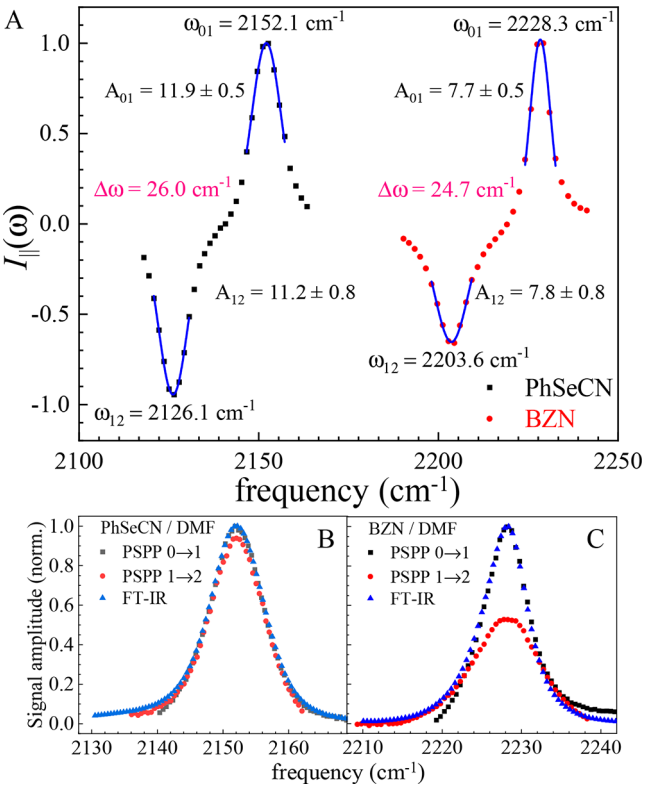

Figure 2. (A) Pump−probe signal of CN stretching mode of PhSeCN and BZN in dimethylformamide. Center frequencies (ω_{ij}) of the transitions are shown near each peak. The area of each feature (A_{ij}) and the anharmonicity of the mode ($\Delta\omega$) for both molecules are also shown. The FT-IR absorption spectrum of the CN stretching mode is shown for (B) PhSeCN and (C) BZN, overlaid with the pump-probe 0 → 1 and 1 → 2 transition line shapes. The 1 → 2 transitions were inverted and shifted by the mode's anharmonicity. In PhSeCN, all three line shapes agree with one another, whereas in BZN, the FT-IR agrees with the 0 → 1 transition line shape, but not with the 1 → 2 transition.

at half-maximum (fwhm) of the 0 → 1 transition in BZN is 6.2 ± 0.1 cm^{-1}, whereas the 1 → 2 transition has an fwhm of 9.9 ± 0.3 cm^{-1} and it has a peak amplitude ~30% lower.

To highlight the line shape differences, the pump−probe signals are compared to the modes' linear absorption spectra. Figure 2B,C shows a comparison of the FT-IR spectra of PhSeCN and BZN to the 0 → 1 and 1 → 2 transition line shapes obtained with pump−probe spectroscopy. The 1 → 2 line shape was translated in frequency by the observed vibrational anharmonicity, and its amplitude was inverted for clarity. For PhSeCN, the linear absorption spectrum matches the line shape of both 0 → 1 and 1 → 2 pump−probe transitions, with a small 0 → 1 intensity difference that will be further explored in subsequent sections. However, for BZN, the linear absorption spectrum matches the 0 → 1 line shape, but not the 1 → 2. The latter transition is much broader than both the FT-IR absorption spectrum and the pump−probe 0 → 1 line shape. Further inspection of the Gaussian fits shows that, for BZN, although the line shapes shown in Figure 2A are different, the integrated areas of the 0 → 1 and 1 → 2 transitions are the same. The fact that the areas are the same shows that the difference in line shapes results from a different spread of vibrational frequencies for the 0 → 1 and 1 → 2 transitions. However, these are two transitions of the same

https://doi.org/10.1021/acs.jpcb.2c06071
J. Phys. Chem. B 2023, 127, 717−731

ensemble of molecules. Since the solvent−solute molecular environments are the same for both transitions, a different spread of frequencies must result from an energy-level-dependent property of the benzonitrile molecule.

The data presented above were collected with a 0.5 ps time delay to avoid any distortions of the line shape due to a previously reported process of intramolecular vibrational relaxation (IVR), which creates a combination band shift that becomes apparent at ∼5 ps.[42] Further, the agreement between the 0 → 1 transition line shape and BZN's FT-IR spectrum shows that there is no signal contamination (Figure 2C). Finally, since the combination band shift is a ground state process,[42] the excited state absorption from |1⟩ to |2⟩ is not affected, and the distinct 1 → 2 line shape cannot be a result of IVR.

IV.C. *E*-Field-Dependent Frequency Shifts and Line Widths. Before exploring the physical origins of the difference in line shape between the 0 → 1 and 1 → 2 transitions in BZN, we characterize the solvatochromic changes experienced by the line shapes as a function of applied external electric field. In the past, the first-order Stark effect was shown to account for the solvatochromic frequency shifts (measured with FT-IR spectroscopy) experienced by nitriles in a variety of solvent environments.[1] The standard method to extract the vibrational sensitivity to electric fields is to collect the linear absorption spectrum of the vibrational mode of interest in a series of solvents of different dielectric constants and calibrating the vibrational transition frequency shift that occurs as a function of the solvent's calculated average electric field (eqs 1 and 2).

We collected the pump−probe signal of the CN stretching vibration of PhSeCN and BZN in ten nonaromatic and non-hydrogen-bonding solvents that span a wide range of polarities from DMSO to hexane. For clarity, Figure 3 shows only four solvents, but the full set of line shapes in ten solvents, and the parameters that describe them, can be found in Sections S2 and S3. The data were normalized to the maximum amplitude of the 0 → 1 transition to highlight differences in the 1 → 2 transition line shape. The signals of both BZN and PhSeCN shift to lower vibrational frequencies with increasing solvent polarity. In hexane, the center vibrational frequency for BZN is 2232.7 and 2160.1 cm^{-1} for PhSeCN. In DMSO, the frequencies are 2227.4 and 2150.3 cm^{-1} for BZN and PhSeCN, respectively.

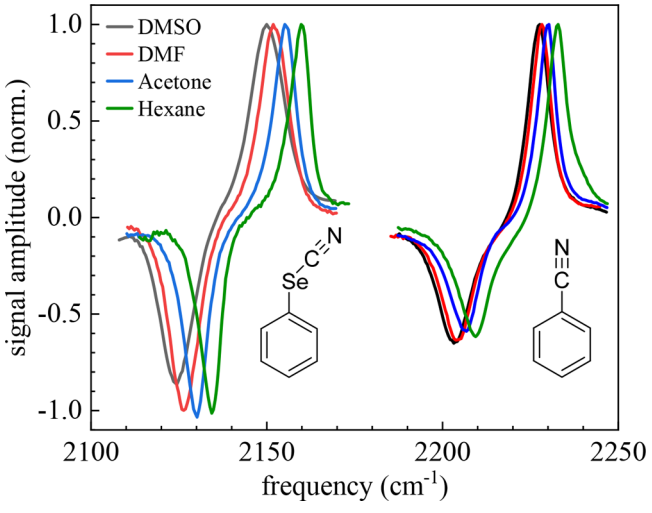

Figure 3. Pump−probe signal for PhSeCN (left) and BZN (right) in four representative solvents, normalized to the maximum amplitude of the 0 → 1 transition. The line shapes of the two transitions are well-behaved in PhSeCN (almost equal amplitudes and widths). In BZN, there are large differences between the two transitions, with the 1 → 2 transition displaying lower amplitudes and larger widths.

The signal obtained from PhSeCN is well-behaved, in the sense that the two transitions have the same spectral shape across most solvents. However, the 1 → 2 transition of PhSeCN in DMSO has a visibly lower amplitude than the 0 → 1 transition. By contrast, the pump−probe signals in all solvents for BZN show large differences between the line shape of the two transitions, with the 1 → 2 transition being broader with less peak amplitude than the 0 → 1 transition. These results demonstrate that the line shape difference is not unique to the BZN/DMF pair shown in Figure 2, and that PhSeCN also displays a similar effect (at least at high field values).

In Figure 4A,C, the center frequencies of the 0 → 1 and 1 → 2 transitions of PhSeCN and BZN were plotted as a function of *E*-field. The 1 → 2 vibrational frequencies were shifted by the observed anharmonicity of the CN mode in hexane. Hexane was chosen as a reference point because it has the lowest *E*-field magnitude of all the solvents, and comparing the data in this way highlights the effect of increasing the solvent *E*-field on the vibrational frequency differences between transitions.

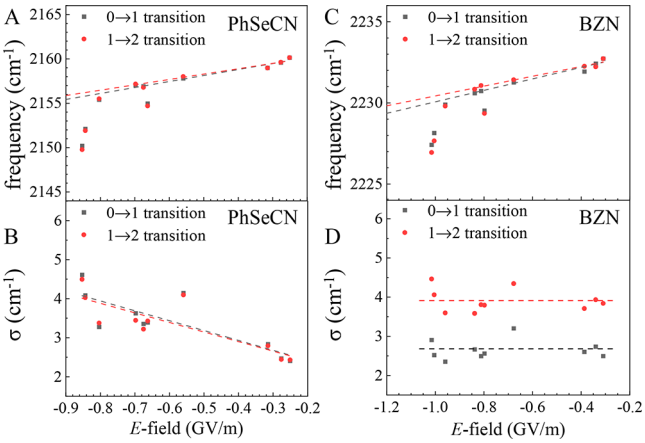

Figure 4. Comparison of the vibrational frequency shift experienced by the 0 → 1 and 1 → 2 transitions in (A) PhSeCN and (C) BZN. The 1 → 2 vibrational frequencies were shifted up by the vibrational anharmonicity of the CN mode in hexane to highlight the effect that increasing the solvent's *E*-field magnitude has on the frequency shifts. Line widths are plotted as the standard deviations of both 0 → 1 and 1 → 2 transitions in PhSeCN (B) and BZN (D) as a function of solvent electric field. In PhSeCN, the two transitions display equal line widths and a field dependence, whereas in BZN, the 1 → 2 transition has 47% wider widths than the 0 → 1 transition line widths and neither transition displays a field dependence. The dashed lines in panels A−C are linear fits to the data, whereas in panel D, the lines represents guides to the eye plotted at the average width of the transition to highlight the field independence in the data. The error bars on these data are too small to be visible in the plot. The center frequencies have an average of ±0.04 and ±0.03 cm^{-1} for PhSeCN and BZN, respectively. The standard deviations have an average of ±0.1 cm^{-1} for both molecules. The exact values of the error bars for each molecule and solvent can be found in Sections S2 and S3 of the Supporting Information.

For PhSeCN (Figure 4A), the vibrational frequencies of the two transitions in most solvents are virtually identical, showing

https://doi.org/10.1021/acs.jpcb.2c06071
J. Phys. Chem. B 2023, 127, 717−731

that there is very little variation in the anharmonicity of the CN vibrational mode as a function of solvent. However, when the *E*-field reaches a magnitude >0.85 GV/m (DMSO and DMF), the difference between the two transitions becomes somewhat more evident, where the shifted 1 → 2 vibrational frequency is slightly lower than the 0 → 1 frequency (i.e., larger anharmonicity). In the case of BZN (Figure 4C), the vibrational frequencies of the two transitions do not coincide for any of the solvents. Analogous to the case of PhSeCN, the data for DMSO and DMF (highest two field magnitudes) show the clearest difference between the two transition frequencies, but BZN displays a larger change in anharmonicity for these two solvents compared to PhSeCN. These observations will be revisited and discussed below in the context of the magnitude of the Stark tuning parameter and NSC to the two vibrational transitions.

The vibrational frequency data for both PhSeCN and BZN do not follow a linear trend as described by eq 1 over the entire range of *E*-fields. The dashed lines in Figure 4A,C show linear fits to the low-field data, extended over the full range of *E*-fields, and demonstrate that the observed field-dependent frequency shifts are not linear at high fields. This has been observed in the past and has been attributed to anharmonicity effects and possibly polarizability contributions.[26,29]

Before exploring the origin of these observations further, it is necessary to discuss the field-dependent trends in the spectral line widths of these transitions. Figure 4B,D shows the standard deviation of the 0 → 1 and 1 → 2 transitions of PhSeCN and BZN as a function of the solvents' electric fields. These results show that while the standard deviations of the two transitions are visibly different in BZN (Figure 4D), they are very similar in PhSeCN (Figure 4B). Considering only the 0 → 1 transitions, for the solvents with the lowest *E*-field magnitudes (hexane and cyclohexane), the 0 → 1 line shapes in both molecules have a standard deviation of ∼2.5 cm^{-1}. However, as the *E*-field magnitude increases, PhSeCN displays a broader width than BZN. While the standard deviation of the transition in PhSeCN increases to ∼4.5 cm^{-1} at the highest *E*-field (DMSO), the standard deviation in BZN remains constant at ∼2.7 cm^{-1}. Even though the widths of both PhSeCN and BZN jump around a lot, PhSeCN widths have a field dependence, while the BZN widths do not (see dashed lines).

The Stark tuning rates of BZN and PhSeCN have been measured before using linear infrared absorption spectroscopy and the linear regression fit method described above.[1,43] It was observed then that PhSeCN has a Stark tuning rate that is ∼2.5× higher, 12.3 $cm^{-1}/(GV/m)$, than that of BZN with 5 $cm^{-1}/(GV/m)$. A recreation of these measurements is shown in Section S9. For the present discussion, it is important that since the set of solvents, and therefore *E*-fields applied to these molecules, are the same, a more sensitive Stark tuning rate will result in a more dramatic environment-dependent vibrational frequency shift for any molecular subensemble, causing the spectrum to have a broader spread of frequencies (wider line width). Therefore, we would expect the line width to increase with increasing *E*-field and the line widths of PhSeCN to be larger than BZN's.

Figure 4B shows that, as expected, the PhSeCN widths grow with increasing *E*-field, but Figure 4D shows that the BZN widths remain unchanged within the spread of line widths. The horizontal lines in Figure 4D are positioned at the average value of the observed spectral widths as guides to the eye to highlight the lack of a field dependence for the 0 → 1 and 1 → 2 transitions.

Considering both molecules' 1 → 2 transitions only, in the low-*E*-field-magnitude solvents (<0.5 GV/m), BZN displays a spectrum that is broader (∼3.9 cm^{-1}) than PhSeCN's (∼2.5 cm^{-1}), whereas above 0.5 GV/m, the fwhm of BZN's 1 → 2 transition is comparable to that of PhSeCN's (∼4.5 cm^{-1}). Once again, the line width of BZN's 1 → 2 transition is field-independent. Moreover, there is a substantial difference in the line widths of the two transitions in BZN, which is not observed for PhSeCN. The fact that BZN has a smaller Stark tuning rate than PhSeCN would suggest that the BZN line widths would be narrower than those of PhSeCN, if the dominant contribution to the BZN line widths were from the VSE. We propose that the field-dependent experimental line width data are the result of two contributions: one arising from the first-order Stark effect (VSE), and one arising from non-Stark intermolecular interactions between the probes and the solvents (NSC). The idea that the VSE is not sufficient to reproduce experimentally measured vibrational frequency shifts has been explored in the past with methyl thiocyanate. In one study, it was demonstrated that van der Waals (VdW) interactions are necessary to accurately reproduce nitrile vibrational line shapes and frequency shifts, where between 11% and 23% of the shift results from VdW effects.[44] Additionally, SolEFP simulations were used to determine that nitrile vibrational frequencies result from an interplay of Coulombic, induction, dispersion, and repulsion interactions, out of which only Coulombic and induction interactions are linearly correlated with the solvent-generated *E*-field.[30] The repulsion contribution to the nitrile frequency in protic solvents is much larger than in aprotic solvents, but dispersion is important in both cases. Separated into interactions that are and are not linearly dependent on the electric field, the field-independent contributions appeared to dominate the distribution of solvent-induced vibrational frequency shifts. Since the origin of the NSC has been identified before, in the next section we focus on the decomposition of the experimental vibrational frequencies and line widths into the magnitude of the VSE and NSC contributions over a wide range of solvent environments and for the two different vibrational transitions.

IV.D. VSE and NSC Line Shape Decomposition. The pump−probe experiment measures an inhomogeneously broadened absorption spectrum that is well-described as a Gaussian function (see Section S2). If the electric field could be switched off while keeping all other intermolecular interactions of the system the same, the mode would have a distribution of frequencies that is uncorrelated with a field-induced frequency shift. The field-free spectrum would be an inhomogeneously broadened Gaussian as a result of non-Stark solute/solvent intermolecular interactions. This assumes that the inhomogeneous broadening is much greater than the homogeneous broadening, which is generally true. Therefore, we model the experimentally measured line shapes in terms of two solvent-dependent but uncorrelated Gaussian functions, with a Stark, $\Omega_S(\omega)$, and an NSC, $\Omega_{NSC}(\omega)$, component. $\Omega_{NSC}(\omega)$ represents the spectrum that the vibrational mode would have in the absence of an electric field but with other probe/solvent intermolecular interactions still active. $\Omega_S(\omega)$ is the field-dependent spectrum in the absence of $\Omega_{NSC}(\omega)$. Each contribution has the form of

https://doi.org/10.1021/acs.jpcb.2c06071
J. Phys. Chem. B 2023, 127, 717−731

Table 1. Stark Contribution Slopes for the Field-Dependent Center Frequency Shift (μ) and Standard Deviation (β) of 0 → 1 and 1 → 2 Transitions of CN Stretch in PhSeCN and BZN

	PhSeCN		BZN	
	0 → 1	1 → 2	0 → 1	1 → 2
μ (cm^{-1}/(GV/m))	7.25 ± 0.6	7.11 ± 0.7	3.57 ± 0.3	3.04 ± 0.3
β (cm^{-1}/(GV/m))	−2.47 ± 0.2	−2.23 ± 0.2	−1.22 ± 0.2[a]	−1.34 ± 0.3[b]

[a]Approximated by decreasing the slope of PhSeCN's 0 → 1 transition by 49% (i.e., difference between slopes for center frequency shift). [b]Approximated by increasing BZN's 0 → 1 slope by 10.5% in agreement with perturbation and DFT calculations (see below).

$$\Omega(\omega) = \frac{1}{\sqrt{2\pi\sigma^2}} e^{-(\omega-\alpha)^2/2\sigma^2} \tag{3}$$

where α and σ represent the center frequency and standard deviation of the spectrum, respectively. The spectrum that results from both contributions is the convolution of the two components

$$\Omega_{conv.}(\omega) = \int_{-\infty}^{\infty} \Omega_S(\omega - \gamma)\, \Omega_{NSC}(\gamma)\, d\gamma \tag{4}$$

ω is the resulting frequency, and γ is an integration variable for the convolution to compute the intensity product of all frequency combinations for the two spectra. The result of the convolution of two Gaussian functions is another Gaussian given by

$$\Omega_{conv.}(\omega) = \frac{1}{\sqrt{2\pi({\sigma_{NSC}}^2 + {\sigma_S}^2)}} \exp\left(\frac{-(\omega - (\alpha_{NSC} + \alpha_S))^2}{2({\sigma_{NSC}}^2 + {\sigma_S}^2)}\right) \tag{5}$$

which is centered at $\alpha_{NSC} + \alpha_S$ and has standard deviation $\sqrt{{\sigma_{NSC}}^2 + {\sigma_S}^2}$.

Equation 5 shows that the center frequency of the NSC component shifts by the center frequency of the Stark component, which is consistent with eq 1; i.e., the center frequency is not affected by the line width, which itself is changing with the E-field. On the other hand, it is the square of the resulting standard deviation that changes linearly with the sum of the squares of the Stark and NSC standard deviations. Therefore, in plots of E-field vs center frequency and E-field vs standard deviation, the rate of change of these two quantities will not be the same; i.e., they will have different slopes unless σ_{NSC} is negligible compared to σ_S. If σ_{NSC} is large compared to σ_S, there will be no field dependence to the line width.

In the absence of the VSE, there are probe/solvent intermolecular interactions that will cause both the frequency and the standard deviation of the NSC spectrum to change with solvent. However, because these interactions do not change systematically with the identity of the solvent the way the field does per eq 2, the NSC frequency and standard deviation dependence do not have an established functional form. The NSC center frequency and standard deviation are each modified by their own unique solvent-dependent scaling factor. Incorporating these factors into eq 5, we obtain a more general convolution expression

$$\Omega_{conv.}(\omega) = \frac{1}{\sqrt{2\pi((\tau_{solv.} \times \sigma_0)^2 + (\beta \times E)^2)}} \exp\left(\frac{-(\omega - ((\varphi_{solv.} \times \alpha_0) - (\mu \times E))^2}{2((\tau_{solv.} \times \sigma_0)^2 + (\beta \times E)^2)}\right) \tag{6}$$

where μ and β are the rate of change of the center frequency and standard deviation, respectively, as a function of field for the Stark contribution. φ_{solv} and τ_{solv} are the unique solvent-dependent frequency and standard deviation scaling factors for the NSC contribution, respectively. α_0 and σ_0 are the zero-field center frequency and standard deviation obtained from the y-intercept of field-dependent plots like those in Figure 4, and E is the solvent-generated electric field magnitude. Equation 6 then represents a Gaussian spectrum whose center and width depend on four independent parameters: μ, β, φ_{solv}, and τ_{solv}. The NSC center frequency and standard deviation are given by $\alpha_{NSC} = \varphi_{solv} \times \alpha_0$ and $\sigma_{NSC} = \tau_{solv} \times \sigma_0$, respectively, whereas the Stark center frequency shift is $\alpha_S = \mu \times E$ and the standard deviation is given by $\sigma_S = \beta \times E$.

It is shown in Section S4 that when the Stark and non-Stark line widths are comparable to each other, the resulting line width increases if either width increases because the total line width is the convolution of the two widths. If one line width is very narrow compared to the other, the resulting line width is given by the broader line width. These considerations will be important below in discussing the differences in line widths of PhSeCN and BZN as a function of electric field.

Using this model, the experimental vibrational frequencies and line widths of the CN stretch were decomposed for each solvent into Stark and NSC components. This analysis was used to show that the NSC component plays an important role in the observed data, and that it is the reason for the deviations from linearity that are commonly observed in the solvatochromic measurements presented in Figure 4.

We begin the analysis with PhSeCN. As discussed above, the data in Figure 4 are expected to be linear by eq 1. However, some of the points clearly miss the linear trend. To approximate a linear field-dependent Stark frequency shift consistent with eq 1, the data points that did not fit the linear trend in Figure 4A,C were removed, and new linear regressions were computed (see Section S4). The slopes used for each transition of PhSeCN and BZN for this model are given in Table 1. Using these slopes, the vibrational frequency shifts and line widths that result from the Stark effect were computed, free from an NSC component, to create a set of 0 → 1 $\Omega_S(\omega)$ spectra.

It is customary to call the y-intercept values of these linear fits the zero-field frequency and width, which describe a single $\Omega_0(\omega)$ spectrum, called the zero-field spectrum. In the context of our model, $\Omega_0(\omega)$ would replace $\Omega_{NSC}(\omega)$ in eq 4 to compute a convolution with $\Omega_S(\omega)$. It is important to highlight, however, that $\Omega_0(\omega)$ and $\Omega_{NSC}(\omega)$ are fundamentally different, although they originate from similar intermolecular interactions. As discussed above, and shown below, the NSC contribution is solvent-dependent, whereas $\Omega_0(\omega)$ is inherently solvent-independent; i.e., a single center frequency and standard deviation are obtained from the y-intercepts. A first iteration of our model uses the $\Omega_0(\omega)$ spectrum to assess how appropriate the notion of a unique and solvent-independent zero-field contribution is. This iteration of the analysis will be referred to as the zero-field model.

https://doi.org/10.1021/acs.jpcb.2c06071
J. Phys. Chem. B 2023, 127, 717−731

Using $\Omega_S(\omega)$ and $\Omega_0(\omega)$, eq 4 was employed to compute a set of Ω_{conv} (ω) spectra (see Section S4). All spectra were fitted to Gaussian functions, and the resulting maximum vibrational frequencies and standard deviations were plotted against the experimentally measured results in Figure 5. In the case of the vibrational frequency (Figure 5A), this model does a reasonable job of reproducing much of the experimental data, particularly at low field. However, there are significant deviations from the experimental data at high field. The results indicate that some of the solvents that produce large electric fields must have substantial NSC contributions, and it shows that a linear Stark shift with a unique zero-field frequency is not sufficient to reproduce the experimental results.

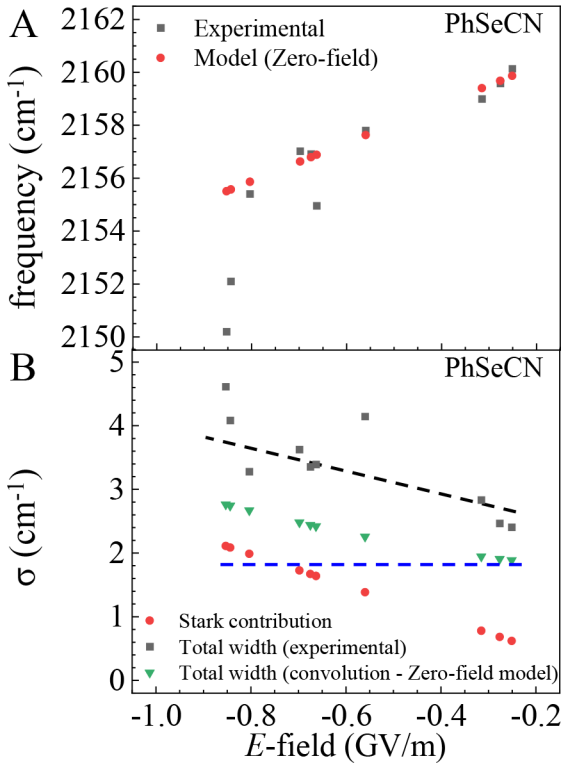

Figure 5. Results of the zero-field model used to decompose the experimental data into a set of solvent-dependent Stark spectra, and a single solvent-independent zero-field spectrum. All spectra were fitted with Gaussian functions, and the individual contributions, as well as the convolution results (eq 6), are displayed against the experimental values for (A) the center frequency and (B) the line width standard deviation. The zero-field standard deviation is shown as a blue horizontal dashed line. The black dashed line is a guide to the eye to emphasize the field dependence of the experimental spectral standard deviation. The model reproduces the low-field center frequency data but fails to capture the high-field nonlinearity. For the line widths, the model does a poor job of reproducing the data and yields line widths that are too small compared to the experimental results across the entire field spectrum.

For the line widths, plotted as their standard deviations in Figure 5B, the zero-field model does a poor job of reproducing the experimental results. The red points are the Stark-only standard deviations, and the green points are the convolution of the Stark-only standard deviations with the zero-field standard deviation (the zero-field model). The blue dashed line is the zero-field standard deviation. At the smallest field magnitude, the Stark contribution is small and the convolved standard deviation is only slightly larger than the zero-field standard deviation. As the field increases, the Stark contribution increases. For the largest field, the convolved standard deviation is significantly larger than the zero-field contribution. The black points are the experimental standard deviations, which show a field dependence that is similar to that of the zero-field model (green points). The black dashed line is an aid to the eye. However, the average value of the data is substantially greater than that given by the zero-field model (green points). In addition, the data have very large deviations from linearity, which are not captured by the zero-field model. These results foreshadow that the NSC contributes significantly to the line widths, and that its contributions vary nonsystematically from solvent to solvent.

We quantify the solvent-dependent field-free spectrum for PhSeCN by tuning both its maximum vibrational frequency and spectral width, solvent by solvent, to reproduce the experimental results, using the previously determined $\Omega_S(\omega)$ set unchanged. This process provides the $\Omega_{NSC}(\omega)$ spectra, which are shown in Figure 6A. The NSC line widths' center

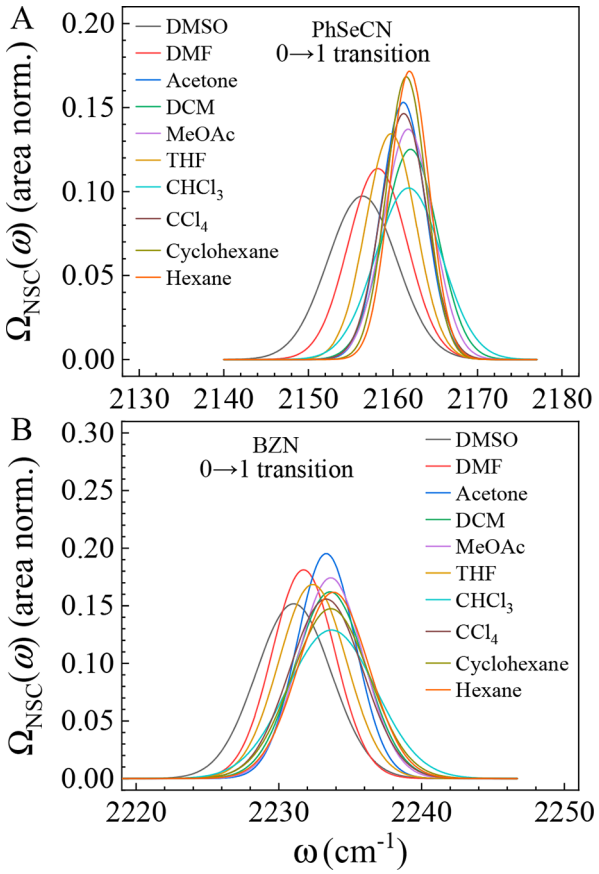

Figure 6. NSC spectra obtained from the NSC model to reproduce the experimental frequency and line width data given linearly field-dependent broadening and shifting Stark spectra for PhSeCN (A) and BZN (B). This model contrasts with the zero-field model on the fundamental nature of the NSC component to both frequency and line width, and it highlights that the NSC must be solvent-dependent and that using a single zero-field frequency and standard deviation parameter is not sufficient to represent the experiments. These spectra show that there are large differences in the NSC spectrum as a function of solvent with changes that are uncorrelated with the field in both center frequencies and widths.

https://doi.org/10.1021/acs.jpcb.2c06071
J. Phys. Chem. B 2023, 127, 717−731

Table 2. Solvent-Dependent Non-Stark Solvent Coupling Contribution (NSC) Center Frequency and Standard Deviations and Zero-Field Contributions for 0 → 1 and 1 → 2 Transitions of CN Stretch in PhSeCN and BZN[a]

	PhSeCN		BZN	
	0 → 1	1 → 2	0 → 1	1 → 2
ω_0 (cm^{-1})	2161.7 ± 0.6	2136.2 ± 0.4	2233.6 ± 0.2	2210.1 ± 0.2
σ_0 (cm^{-1})	1.78 ± 0.1	1.85 ± 0.1	–[b]	–[b]

	PhSeCN				BZN			
	0→1		1→2		0→1		1→2	
	$\varphi_{solv} \times \omega_0$	$\tau_{solv} \times \sigma_0$	$\varphi_{solv} \times \omega_0$	$\tau_{solv} \times \sigma_0$	$\varphi_{solv} \times \omega_0$	$\tau_{solv} \times \sigma_0$	$\varphi_{solv} \times \omega_0$	$\tau_{solv} \times \sigma_0$
DMSO	2156.4	4.10	2130.4	3.93	2231.0	2.63	2206.7	4.25
DMF	2158.2	3.51	2132.4	3.39	2231.7	2.20	2207.3	3.83
Acetone	2161.2	2.61	2135.7	2.67	2233.3	2.04	2209.3	3.36
DCM	2162.1	3.19	2136.6	2.94	2233.6	2.46	2210.0	3.40
MeOAc	2161.8	2.91	2133.9	2.73	2233.6	2.29	2210.2	3.65
THF	2159.8	2.97	2136.1	2.96	2232.4	2.37	2208.4	3.64
$CHCl_3$	2161.9	3.91	2136.5	3.84	2233.7	3.09	2210.1	4.25
CCl_4	2161.3	2.72	2135.7	2.67	2233.3	2.56	2210.1	3.67
Cyclohexane	2161.6	2.37	2136.1	2.34	2233.6	2.71	2209.9	3.91
Hexane	2162.0	2.33	2136.4	2.34	2233.8	2.47	2210.3	3.82

[a]Final center frequencies and standard deviations are given because scaling factors cannot be determined for the standard deviation of BZN. [b]It was not possible to obtain a single zero-field standard deviation for BZN because neither transition displayed a field dependence (Figure 4).

frequencies and standard deviations are presented in Table 2. The Stark contribution increases linearly with increasing *E*-field, whereas the NSC contributions vary to generate the experimentally observed spectra (see Section S4). The $\Omega_S(\omega)$ and the new varying spectral set $\Omega_{NSC}(\omega)$ were then convolved (eq 4) to obtain a new set of $\Omega_{conv}(\omega)$. This procedure is referred to as the NSC model. The results were fitted using a Gaussian function, and the individual Stark and NSC contributions to the vibrational frequency and the spectral standard deviation were plotted together with the experimental results in Figure 7A,B for PhSeCN. The agreement between the model (green triangles) and the experimental data (open blue circles) is perfect (the data fall on top of each other) because the parameters that describe $\Omega_{NSC}(\omega)$ were chosen to reproduce the experimental data exactly. What is important in this analysis is not the agreement between the final values provided by the NSC model and the experimental data but, instead, that the parameters that describe the $\Omega_{NSC}(\omega)$ spectra are required to be solvent-dependent for the model to reproduce the experimental results. It is important to note that while the NSC contributions are plotted as a function of *E*-field, these interactions are strictly non-Stark effect interactions and do not result from a vibrational response to a monotonically changing electric field. These results are plotted as a function of *E*-field simply to illustrate how they add to the individual linear Stark effect contributions in a solvent-dependent manner to generate the experimental data. The frequencies and standard deviations for $\Omega_{NSC}(\omega)$ demonstrate that the experimental data contain a significant contribution from non-Stark effect intermolecular interactions. The NSC contributions depend on complex solute−solvent interactions[30] and provide the shape of the field-dependent trends and all departures from linearity.

The same procedure described above was used to decompose the experimental data obtained for BZN. The case of a unique $\Omega_0(\omega)$ was not considered for BZN because it was shown previously with PhSeCN that a solvent-dependent $\Omega_{NSC}(\omega)$ is required to reproduce the experimental results. A linear subset of the field-dependent center frequency data was

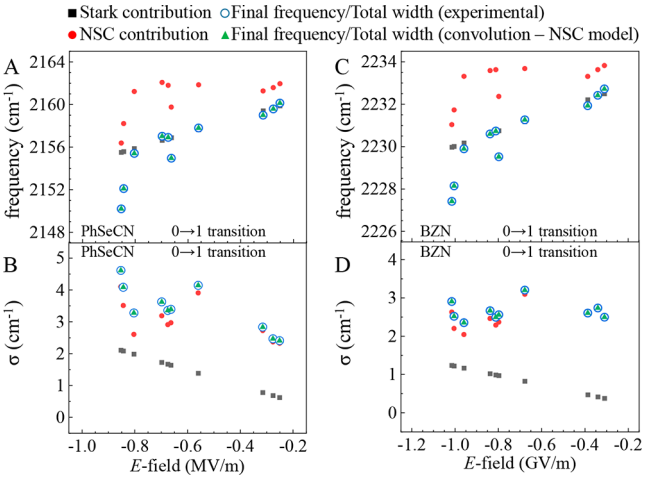

Figure 7. Results of the NSC model used to decompose the 0 → 1 transition experimental data into a Stark and an NSC component for the center frequency shifts and line widths (as standard deviations) of PhSeCN (A, B) and BZN (C, D). The figure presents the individual Stark and NSC components, the final frequencies and total widths predicted by the convolution model, and the experimentally measured frequencies and widths for each solvent. These results highlight that while the Stark component increases linearly with field magnitude, it is the NSC that provides the overall shape of the data and the departures from linearity. In the case of BZN's width, the NSC completely overwhelms the Stark width and eliminates a field dependence.

used to determine the parameters that describe the linear change in the vibrational frequency of the CN stretch (see Section S4). The slope for these data is 3.57 cm^{-1}/(GV/m), which is 49% lower than the 7.25 cm^{-1}/(GV/m) obtained for PhSeCN (Table 1). This difference is in agreement with previous measurements of the Stark tuning rate of the CN mode of these two molecules.[1,28] Since the line width data obtained from BZN do not display a field dependence (Figure 4), it is not possible to obtain a linear equation that describes a field-dependent spectral width. Instead, this value was

https://doi.org/10.1021/acs.jpcb.2c06071
J. Phys. Chem. B 2023, 127, 717−731

approximated by taking the slope obtained for the field-dependent standard deviations in PhSeCN and reducing it by 49% (the same difference between the slopes of the two molecules' field-dependent frequencies). The resulting slope was then used to approximate the linear field-dependent line widths for BZN.

With these two linear regressions, $\Omega_S(\omega)$ and $\Omega_{NSC}(\omega)$ spectral sets were generated for BZN to reproduce the experimental data. The NSC spectra are presented in Figure 6B, whereas the Stark and convolution spectra are shown in Section S4. The standard deviation and center frequency parameters that describe the Stark, NSC, and cumulative NSC model spectra are plotted against the experimental data in Figure 7C,D. As with PhSeCN, the Stark contribution to the center frequency (Figure 7C) increases linearly with increasing electric field, but less rapidly than in PhSeCN due to BZN's lower Stark tuning rate, whereas the NSC contribution varies to generate the experimental data. The NSC spectra for BZN are significantly broader than those for PhSeCN. In the case of the vibrational frequencies, the solvent-dependent $\Omega_{NSC}(\omega)$ frequency traces the overall shape of the experimental data, and it displays the characteristic nonlinearity observed at high electric fields. This is analogous to the results for PhSeCN, confirming that the NSC component appears to be responsible for the shape of the field-dependent data. The incorporation of a solvent-dependent NSC allows the model to capture the strongly nonlinear behavior of the data at high field. The Stark effect acts as a small offset for each data point that lowers the NSC vibrational frequency in an *E*-field-dependent manner, as is expected by eq 1.

The NSC contributions completely dominate the line widths of BZN. The standard deviations are shown in Figure 7D. The NSC standard deviations (red circles) are at least twice and as much as six times larger than the Stark contribution (black squares), which causes the experimental standard deviations to almost have the value of the NSC alone. This is apparent by comparing the agreement between the experimental standard deviation and the NSC standard deviation in the low-field regime, where the Stark contribution is the smallest. The experimental values (open blue circles) and the NSC values agree perfectly. The red circles are hidden behind green triangles. As the Stark contribution grows linearly with *E*-field, it becomes visible in addition to the NSC to generate the experimental standard deviations, but the Stark contribution is not large enough to induce a field dependence in the data. The NSC contribution does not change monotonically with the identity of the solvent, but rather it jumps around; it dominates the observed spectral widths, resulting in a complete loss of the *E*-field dependence of the standard deviation (see Figure 4D).

The analysis presented above provides insights into the origin of observed center frequencies and line widths. It demonstrates that the field-dependent peak positions are independent of the line widths, even when the NSC contribution dominates the latter. It also shows that when the Stark tuning rate is comparable to the NSC contributions, as is the case with PhSeCN, the line widths have a field dependence, albeit with major NSC-induced excursions from linearity. However, when the Stark tuning rate is small relative to the NSC, as with BZN, the line widths are field-independent.

Finally, this same analysis was performed on the peak frequencies and the line widths' standard deviations of the 1 → 2 transition of PhSeCN and BZN. The details of the spectra are shown in Sections S2 and S3. A field dependence is observed for both the frequency and the standard deviation in the 1 → 2 transition for PhSeCN. Therefore, the same analysis used for the 0 → 1 transition data was repeated. Because no field dependence is observed in the standard deviation for BZN, a linear regression cannot be performed. There is one small caveat in this case that needs to be considered. In subsequent sections, it will be shown that the Stark tuning rate of the 1 → 2 transition is slightly larger than that of the 0 → 1 transition, that the change in rate is molecule-dependent, and that it is larger in BZN. To incorporate this result into the line shape decomposition analysis, the slope of the line that would describe the field-dependent standard deviation of BZN in the 1 → 2 transition was approximated by taking the slope from the 0 → 1 transition and increasing it by 10.5% (i.e., the calculated increase for the Stark tuning rate of BZN's 1 → 2 transition over the 0 → 1 transition).

With a set of $\Omega_S(\omega)$ and $\Omega_{NSC}(\omega)$ for the 1 → 2 transition of both molecules, a set of $\Omega_{conv}(\omega)$ spectra were computed, and the results are shown, together with the experimental data, in Figure 8. For PhSeCN, because there is not a large

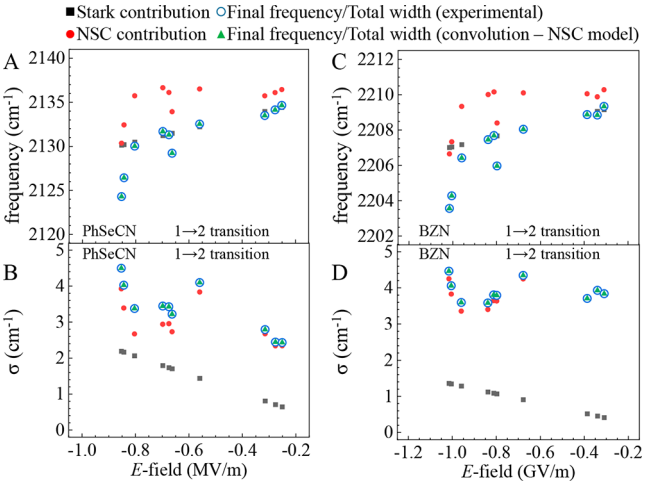

Figure 8. Results of the NSC model used to decompose the 1 → 2 transition experimental data into a Stark and an NSC component for the center frequency shifts and line widths of PhSeCN (A, B) and BZN (C, D). The figure presents the individual Stark and NSC components, the final frequencies, total widths predicted by the convolution model, and the experimentally measured frequencies and widths for each solvent. Analogous to the 0 → 1 transition results, the Stark component increases linearly with field magnitude, but it is the NSC that provides the overall shape of the data and the departures from linearity. The NSC amplitude is much larger in BZN for this transition, while its magnitude remains largely unchanged in PhSeCN, causing the field dependence of the BZN width to be completely lost.

difference between the data obtained for the 0 → 1 and 1 → 2 transitions, the results are very similar to those presented in Figure 7. The NSC contributions to both the frequency and standard deviation provide the overall shape and departures from linearity of the field-dependent center frequency and widths, whereas the Stark contribution produces a small linear shift to the vibrational frequency and a small contribution to the overall standard deviation relative to the 0 → 1 transition.

For BZN, the NSC contribution to the vibrational frequency captures the nonlinearity of the data in a manner analogous to PhSeCN. For the BZN line widths, the NSC accounts for almost all the observed widths, with only a small contribution

https://doi.org/10.1021/acs.jpcb.2c06071
J. Phys. Chem. B 2023, 127, 717−731

from the Stark effect. Two factors can contribute to having significantly larger 1 → 2 than 0 → 1 line widths: a larger Stark tuning rate and a larger NSC. The Stark tuning rate is larger for the 1 → 2 transition but only to a small extent ∼10% (see Section IV.E). The major factor is that the NSC contribution to the spectra becomes significantly larger for the 1 → 2 transition. The line widths of the NSC spectra are so large that the increases in widths from the Stark contributions are almost imperceptible. The large NSC contributions result in no field dependence for the standard deviation, in the same manner as in the 0 → 1 transition.

To quantify the extent to which the NSC dominates the line widths in PhSeCN and BZN, Figure 9 shows the ratio of the

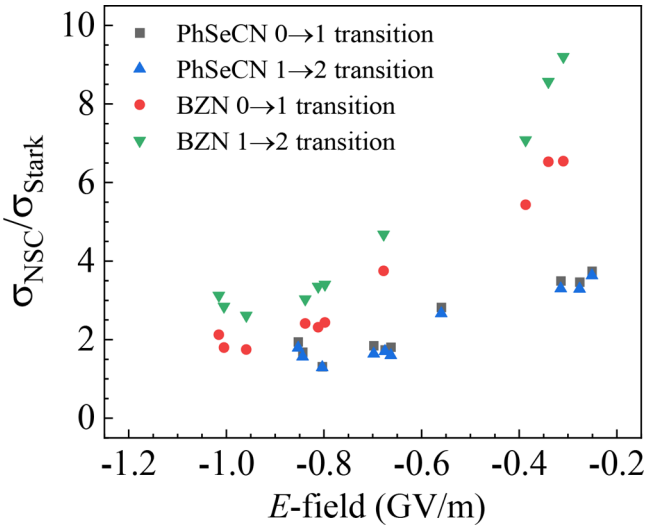

Figure 9. Ratio of the NSC to Stark standard deviation contribution for PhSeCN and BZN in both 0 → 1 and 1 → 2 transitions. The ratio of the two contributions does not change significantly in PhSeCN across transitions, whereas there is a significant increase in the ratio for BZN in the 1 → 2 transition compared to its 0 → 1 transition. These results show that the NSC can depend on which energy level is involved in the vibrational transition.

NSC to Stark widths for both vibrational transitions. The NSC to Stark contribution ratio in BZN increases in the excited state transition, whereas in PhSeCN, it remains almost unchanged. These results show that the NSC is substantially larger for BZN than for PhSeCN, and that the NSC for BZN is much larger for the 1 → 2 transition than for the 0 → 1 transition. This increase in BZN but not PhSeCN can also be seen by comparing the data in Figures 7 and 8. A field dependence is observed in the line widths of PhSeCN, but not in BZN, because the PhSeCN stark tuning rate is substantially larger than BZN's, and its NSC is smaller. In BZN, the NSC width overwhelms the Stark component and eliminates the field dependence.

The difference in the magnitude of the NSC contribution to the line widths in BZN vs PhSeCN is likely related to the presence of the selenium atom in PhSeCN. The selenium makes the CN stretching vibration essentially a local mode, eliminating cross-conjugation with the phenyl ring. Therefore, there is little contribution from solvent−solute interactions with the benzene moiety in PhSeCN. In BZN, the mode that gives rise to the CN absorption spectrum contains substantial amplitude of benzene ring atoms (see Sections S1 and S7). Therefore, interactions between the benzene ring and the solvent will also influence the CN frequency and can contribute to larger inhomogeneously broadened line widths. Finally, in Section S8, pump−probe spectra of the CN stretching vibration of a series of *p*-substituted benzonitrile structures are given. All show the increase in line widths between the 0 → 1 and 1 → 2 transitions as BZN, which suggests the observations made above are general to more chemical structures.

IV.E. Increased Stark Tuning Rate: Perturbation and Density Functional Theory. As discussed above, the first-order VSE arises because the two energy levels involved in the transition have different projection magnitudes of the permanent dipole moment onto the bond axis of interest. Considering the pump−probe signals in Figure 2, the 0 → 1 transition involves the same two levels as the FT-IR spectrum, |0⟩ and |1⟩, so the two line shapes are identical (Figure 2B,C). However, the relevant permanent dipole moment projections for the 1 → 2 transition are those of states |1⟩ and |2⟩. The Stark tuning rate and line widths are then determined by the difference in dipole projection in the first and second excited states. It is interesting to consider if the Stark tuning rate is different for the two transitions studied in the experiments. Based on the decomposition analysis presented above, if there is a difference, it is small. In this section, we explore theoretically the possibility that the difference in spectral width occurs due to variations in the Stark tuning rate for different transitions and the reason that the Stark coupling is substantially larger for the CN mode in PhSeCN than in BZN. Second-order perturbation theory was used to obtain analytical expressions for the wave functions of states |0⟩, |1⟩, and |2⟩ for both molecules. We employed a harmonic oscillator potential with a cubic perturbation as follows:

$$v(x) = \frac{1}{2}kx^2 - qx^3 \tag{7}$$

We used the harmonic oscillator raising and lower operator representation, which makes the calculations of the expressions for the energies and the superposition of harmonic oscillator states that are the approximate states of the system straightforward (see eqs S1−S4 in Section S6). This approach was used because the only two unknowns in the problem are the harmonic and cubic spring constants, k and q. Since we know the 0 → 1 and 1 → 2 transition energies from the experiments, these two constants were obtained accurately by

Table 3. Experimentally Determined Zero-Field Vibrational Transition Frequencies for 0 → 1 and 1 → 2 Transitions of the CN Stretching Mode in BZN and PhSeCN, Corresponding Vibrational Anharmonicities, and Harmonic and Cubic Spring Constants Used in Second-Order Nondegenerate Perturbation Theory

molecule	$\omega_{0\to1}$ (cm^{-1})	$\omega_{1\to2}$ (cm^{-1})	$\Delta\omega$ (cm^{-1})	k (×10^3 J/m^2)	q (×10^{13} J/m^3)
BZN	2234.6	2211.5	23.1	1.942	1.493
PhSeCN	2163.5	2138.2	25.3	1.825	1.648

https://doi.org/10.1021/acs.jpcb.2c06071
J. Phys. Chem. B 2023, 127, 717−731

fitting the transition energies and anharmonicity using eqs S5 and S9 (see Table 3). Knowing the spring constants, we then used a superposition of Schrödinger representation wave functions (see eq S6) to obtain the probability amplitudes and the desired position-dependent probabilities for each of the three states. Knowing k and q also gives us the approximate potential using eq 7.

The results discussed above were then combined with density functional theory to calculate the change in molecular dipole projection magnitude for the 0 → 1 and 1 → 2 transitions for the two molecules (see Section S6). A related perturbation theory treatment was performed before.[29] However, that treatment was focused on deriving expressions for the expectation value of the bond length in states |0⟩ and |1⟩, and it did not include DFT calculations. This is appropriate for a diatomic (or a perfect local mode), as the molecular dipole change will trace the level-dependent lenghthening of the bond. The method presented here does not assume that the CN vibration is a local mode, and it includes the geometrical and electron density distribution changes that occur in the polyatomic molecule upon vibrational excitation. Another similar treatment was performed to develop a DFT and quantum mechanical approach to calculate the Stark tuning rate and polarizability changes of the 0 → 1 transition with remarkable accuracy.[45] However, that work required expensive computational methods, and it did not explore the changes in Stark tuning rate for higher energy-level transitions. The treatment presented here has the advantage that it is straightforward, general, and computationally inexpensive.

The details of the density functional theory are given in Sections III.C and Section S1. Figure 10 shows that DFT and perturbation theory yield quantitatively equivalent potential energy surfaces up to the energy of the second excited state and demonstrates that it is appropriate to combine the two types of calculations to perform the desired dipole projection weighting calculations (see below). Figure 10 also shows the square of the wave functions for each energy level. The probability of the wave function at each energy level extends out farther for PhSeCN compared to BZN because its potential is more anharmonic.

The details of calculating the dipole moments for each energy level for both molecules are given in Section S6. Briefly, DFT calculations were used to determine the dipole moment as a function of displacement along the normal mode coordinate. At each position, x, the dipole is projected onto the CN bond vector and is weight-averaged by the value of the square of the normalized wave function (probability), $|\Psi_i(x)|^2$ (see Figure 10).

This analysis was repeated for the two molecules. The results are presented in Table 4. The method yielded a ground state permanent dipole moment of 4.6 and 4.3 D for BZN and PhSeCN, respectively. The experimental values previously reported are 4.2 and 4.0 D for BZN and PhSeCN, respectively, and show that our method is reasonably accurate, and the ratios of the dipole moments is quite good.[1,43] The percent change in the projection of the dipole moment between states |0⟩ and |1⟩ in BZN is 0.229%, while in PhSeCN it is 0.311%. This value represents the Stark tuning rate of the molecules' 0 → 1 transition. The calculation predicts that PhSeCN has a 37% larger Stark tuning rate than BZN, which is somewhat lower than the previous reports of a 49% difference[1,43] but in reasonable agreement.

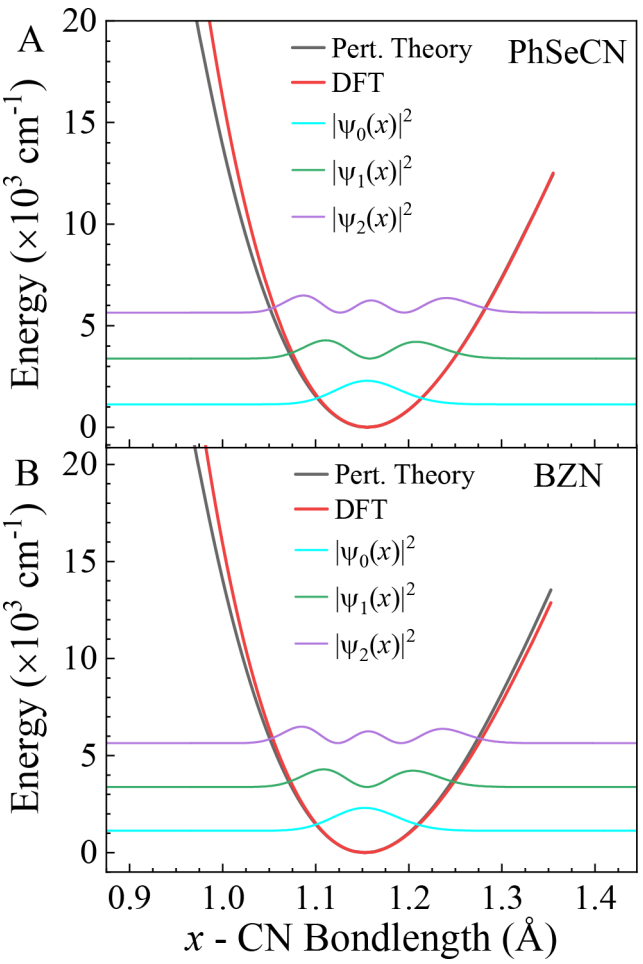

Figure 10. Potential energy surface (PES) of the CN stretching mode in (A) PhSeCN and (B) BZN calculated with density functional theory using a relaxed scan (red trace). The DFT results are compared to the potential energy surface obtained from second-order perturbation theory using a cubic perturbation (black trace). The perturbation was performed to second order on both the eigenvalues and eigenstates. The PES from perturbation theory was determined by varying the harmonic and cubic spring constants to reproduce the experimentally measured vibrational energy transitions and observed anharmonicities. The same constants were used to generate anharmonic wave functions for each energy level. The wave function probabilities are shown for the first three energy levels. The PES obtained from DFT and perturbation theory display a quantitative agreement over the range of energy levels relevant to this study (n = 2).

Table 4. Permanent Dipole Moments, Dipole Moment Projections, and Percent Changes as a Function of Vibrational Transition for Both PhSeCN and BZN Calculated Using a Combination of Perturbation Theory and DFT

	PhSeCN			BZN		
energy level	0	1	2	0	1	2
μ (D)	4.254	4.266	4.280	4.598	4.609	4.621
$\mu_{proj,CN}$ (D)	3.775	3.787	3.799	4.598	4.609	4.621
$\Delta\mu_{proj,CN}$ (%)		0.311	0.330		0.229	0.252
$\Delta\mu_{proj,CN,12}$ (%)			6.5			10.5

The important feature of these calculations is that they can be used to determine the difference in the Stark tuning rates

https://doi.org/10.1021/acs.jpcb.2c06071
J. Phys. Chem. B 2023, 127, 717−731

for the 0 → 1 and the 1 → 2 transitions. The percent increase in the Stark tuning rate between 0 → 1 and 1 → 2 transitions for BZN is 10.5% and 6.5% for PhSeCN. The Stark tuning rate, like the NSC, is sensitive to the vibrational energy levels involved in the transition under study. However, for the two nitriles studied here, the difference in the Stark tuning rates is too small to be evident in the experiments. The large NSC is also likely responsible for obscuring any indications of a field-dependent anharmonicity in Figure 4A,C and is the reason the anharmonicity cannot be used to experimentally identify changes in the Stark tuning rate in higher energy-level transitions. In other systems, the Stark tuning rate increase with higher transitions may be larger and the NSC may be small, in which case the transition-dependent Stark tuning rate could be manifested as an increased line width for the high transition and an increase in the *E*-field-dependent peak shifts. In general, both the transition-dependent NSCs and the transition-dependent Stark tuning rates can contribute to solvent-dependent anharmonicities.

Solvent-independent anharmonicities have been observed for carbonyl stretching modes using two-dimensional infrared experiments.[46] These experiments were used to show that solvent-dependent vibrational frequency shifts do not result from polarizability changes to the chemical bond between the ground and first excited states, but rather from the first-order Stark effect. In these carbonyl systems, deviations were observed from linearity for high-*E*-field solvents like DMSO and DMF, suggesting that the observations made here, that the NSC plays a role in determining vibrational frequencies and line widths, are a general effect, albeit with a different magnitude for different functional groups.

V. CONCLUDING REMARKS

We used FT-IR and infrared pump−probe spectroscopy to access the absorption lines of the CN stretch vibration of BZN and PhSeCN for both the 0 → 1 and 1 → 2 transitions. The two nitriles were studied in the context of the vibrational Stark effect in ten solvents. Changes in the peak shifts and line widths with solvent were measured for both transitions. These two molecules are useful because BZN has a smaller Stark tuning rate but a larger non-Stark coupling to solvents than PhSeCN. In general, line widths are not considered in determining the Stark tuning rate. It was shown here with a theoretical model that incorporating a field-free line width and a linearly increasing, field-dependent line width does not affect the solvent-dependent center frequencies of the spectra; i.e., the peak positions still change linearly with the electric field.

It was determined by experiment that the PhSeCN line widths increase with increasing electric field, but the BZN line widths do not. In addition, the peak positions of both molecules have substantial deviations from increasing linearly with the electric field. These observations are caused by non-Stark coupling contributions to both the peak positions and the line widths, which result from solute−solvent interactions, such as van der Waals and repulsive interactions, which are not linearly dependent on the surrounding *E*-field.

Because PhSeCN has a factor of 2.5 larger Stark tuning rate and a smaller NSC than BZN, in the PhSeCN/solvent systems, the Stark coupling dominates the NSC in determining the line widths. Therefore, PhSeCN shows an approximately linear increase in line width with increasing electric field, although there are substantial deviations around the line. In the BZN/solvent systems, the line widths are dominated by the NSC, which is not correlated with the electric field. Therefore, BZN does not display an increase in line width with increasing electric field but does show major line width variations around an average value.

A similar analysis to the one outlined in this paper can be applied to any vibrational probe/solvent system, where one of the main markers of a significant NSC contribution is a prominent difference in the line shape of the 0 → 1 and 1 → 2 vibrational transitions. Qualitatively similar observations to those made on BZN were made on BZN derivatives (Section S8), which suggests that these observations and models are general.

The experiments and theory presented here highlight important aspects of the VSE. Vibrational mode frequency shifts and, to a greater extent, line widths can be significantly affected, and even dominated, by non-Stark solvent coupling contributions, which combine with the linear electric field Stark coupling. These NSC effects can change the apparent Stark tuning rate or affect the determination of electric fields in condensed phase chemical systems. Our results also show that the combination of contributions becomes more important as higher energy-level transitions are accessed because of energy-level-dependent changes in both Stark and NSC components.

■ ASSOCIATED CONTENT

Supporting Information

The Supporting Information is available free of charge at https://pubs.acs.org/doi/10.1021/acs.jpcb.2c06071.

> Density functional theory calculations, solvent-dependent pump−probe signals, spectrum decomposition model, FT-IR spectra, perturbation theory, Mulliken atomic charges, examples of other chemical structures with the same effect as BZN, and extraction of Stark tuning rates using the standard solvatochromic method (PDF)

■ AUTHOR INFORMATION

Corresponding Author

Michael D. Fayer − *Department of Chemistry, Stanford University, Stanford, California 94305, United States;* orcid.org/0000-0002-0021-1815; Phone: 650 723-4446; Email: fayer@stanford.edu

Authors

Sebastian M. Fica-Contreras − *Department of Chemistry, Stanford University, Stanford, California 94305, United States;* orcid.org/0000-0003-4177-8436

Aaron P. Charnay − *Department of Chemistry, Stanford University, Stanford, California 94305, United States;* orcid.org/0000-0003-1797-9465

Junkun Pan − *Department of Chemistry, Stanford University, Stanford, California 94305, United States;* orcid.org/0000-0001-6128-1844

Complete contact information is available at: https://pubs.acs.org/10.1021/acs.jpcb.2c06071

Author Contributions

S.M.F.-C. designed and performed experiments, did theoretical analysis, and wrote the paper. A.P.C. performed experiments and assisted with theoretical analysis. J.P. performed experiments. M.D.F. did theoretical analysis and wrote the paper.

https://doi.org/10.1021/acs.jpcb.2c06071
J. Phys. Chem. B 2023, 127, 717−731

Notes

The authors declare no competing financial interest.

■ ACKNOWLEDGMENTS

We thank Dr. Kimberly Carter-Fenk and Dr. Kevin Carter-Fenk for providing valuable advice for performing DFT calculations. This work was supported by Office of Naval Research Grant N00014-17-1-2656.

■ REFERENCES

(1) Levinson, N. M.; Fried, S. D.; Boxer, S. G. Solvent-Induced Infrared Frequency Shifts in Aromatic Nitriles are Quantitatively Described by the Vibrational Stark Effect. *J. Phys. Chem. B* **2012**, *116*, 10470−10476.

(2) Fried, S. D.; Boxer, S. G. Measuring Electric Fields and Noncovalent Interactions Using the Vibrational Stark Effect. *Acc. Chem. Res.* **2015**, *48*, 998−1006.

(3) Verma, N.; Tao, Y.; Zou, W.; Chen, X.; Chen, X.; Freindorf, M.; Kraka, E. A Critical Evaluation of Vibrational Stark Effect (VSE) Probes with the Local Vibrational Mode Theory. *Sensors (Basel)* **2020**, *20*, 2358.

(4) Fafarman, A. T.; Webb, L. J.; Chuang, J. I.; Boxer, S. G. Site-Specific Conversion of Cysteine Thiols into Thiocyanate Creates an IR Probe for Electric Fields in Proteins. *J. Am. Chem. Soc.* **2006**, *128*, 13356−13357.

(5) Bagchi, S.; Fried, S. D.; Boxer, S. G. A Solvatochromic Model Calibrates Nitriles' Vibrational Frequencies to Electrostatic Fields. *J. Am. Chem. Soc.* **2012**, *134*, 10373−10376.

(6) Blasiak, B.; Londergan, C. H.; Webb, L. J.; Cho, M. Vibrational Probes: From Small Molecule Solvatochromism Theory and Experiments to Applications in Complex Systems. *Acc. Chem. Res.* **2017**, *50*, 968−976.

(7) Stafford, A. J.; Ensign, D. L.; Webb, L. J. Vibrational Stark Effect Spectroscopy at the Interface of Ras and Rap1A Bound to the Ras Binding Domain of RalGDS Reveals an Electrostatic Mechanism for Protein-Protein Interaction. *J. Phys. Chem. B* **2010**, *114*, 15331−15344.

(8) Slocum, J. D.; Webb, L. J. Measuring Electric Fields in Biological Matter Using the Vibrational Stark Effect of Nitrile Probes. *Annu. Rev. Phys. Chem.* **2018**, *69*, 253−271.

(9) Laberge, M. Intrinsic Protein Electric Fields: Basic Non-Covalent Interactions and Relationship to Protein-Induced Stark Effects. *Biochim. Biophys. Acta* **1998**, *1386*, 305−30.

(10) Prakash, M. K.; Marcus, R. A. An Interpretation of Fluctuations in Enzyme Catalysis Rate, Spectral Diffusion, and Radiative Component of Lifetimes in Terms of Electric Field Fluctuations. *Proc. Natl. Acad. Sci. U.S.A.* **2007**, *104*, 15982−15987.

(11) Adhikary, R.; Zimmermann, J.; Romesberg, F. E. Transparent Window Vibrational Probes for the Characterization of Proteins With High Structural and Temporal Resolution. *Chem. Rev.* **2017**, *117*, 1927−1969.

(12) Lehle, H.; Kriegl, J. M.; Nienhaus, K.; Deng, P.; Fengler, S.; Nienhaus, G. U. Probing Electric Fields in Protein Cavities by Using the Vibrational Stark Effect of Carbon Monoxide. *Biophys. J.* **2005**, *88*, 1978−90.

(13) Slocum, J. D.; First, J. T.; Webb, L. J. Orthogonal Electric Field Measurements near the Green Fluorescent Protein Fluorophore through Stark Effect Spectroscopy and pKa Shifts Provide a Unique Benchmark for Electrostatics Models. *J. Phys. Chem. B* **2017**, *121*, 6799−6812.

(14) Baker, N. A.; Sept, D.; Joseph, S.; Holst, M. J.; McCammon, J. A. Electrostatics of Nanosystems: Applications to Microtubules and the Ribosome. *Proc. Natl. Acad. Sci. U.S.A.* **2001**, *98*, 10037−10041.

(15) Kearney, C.; Olenginski, L. T.; Hirn, T. D.; Fowler, G. D.; Tariq, D.; Brewer, S. H.; Phillips-Piro, C. M. Exploring Local Solvation Environments of a Heme Protein Using the Spectroscopic Reporter 4-Cyano-L-Phenylalanine. *RSC Adv.* **2018**, *8*, 13503−13512.

(16) Fica-Contreras, S. M.; Hoffman, D. J.; Pan, J.; Liang, C.; Fayer, M. D. Free Volume Element Sizes and Dynamics in Polystyrene and Poly(methyl methacrylate) Measured with Ultrafast Infrared Spectroscopy. *J. Am. Chem. Soc.* **2021**, *143*, 3583−3594.

(17) Fried, S. D.; Wang, L. P.; Boxer, S. G.; Ren, P.; Pande, V. S. Calculations of the Electric Fields in Liquid Solutions. *J. Phys. Chem. B* **2013**, *117*, 16236−48.

(18) Zhang, S.; Shi, R.; Ma, X.; Lu, L.; He, Y.; Zhang, X.; Wang, Y.; Deng, Y. Intrinsic Electric Fields in Ionic Liquids Determined by Vibrational Stark Effect Spectroscopy and Molecular Dynamics Simulation. *Chem.—Eur. J.* **2012**, *18*, 11904−11908.

(19) Eaves, J. D.; Tokmakoff, A.; Geissler, P. L. Electric Field Fluctuations Drive Vibrational Dephasing in Water. *J. Phys. Chem. A* **2005**, *109*, 9424−9436.

(20) Lee, H.; Choi, J. H.; Cho, M. Vibrational Solvatochromism and Electrochromism of Cyanide, Thiocyanate, and Azide Anions in Water. *Phys. Chem. Chem. Phys.* **2010**, *12*, 12658−69.

(21) Lambert, D. K. Vibrational Stark Effect of Adsorbates at Electrochemical interfaces. *Electrochim. Acta* **1996**, *41*, 623−630.

(22) Baldelli, S. Surface Structure at the Ionic Liquid-Electrified Metal Interface. *Acc. Chem. Res.* **2008**, *41*, 421−431.

(23) Ge, A.; Videla, P. E.; Lee, G. L.; Rudshteyn, B.; Song, J.; Kubiak, C. P.; Batista, V. S.; Lian, T. Interfacial Structure and Electric Field Probed by in Situ Electrochemical Vibrational Stark Effect Spectroscopy and Computational Modeling. *J. Phys. Chem. C* **2017**, *121*, 18674−18682.

(24) Staffa, J. K.; Lorenz, L.; Stolarski, M.; Murgida, D. H.; Zebger, I.; Utesch, T.; Kozuch, J.; Hildebrandt, P. Determination of the Local Electric Field at Au/SAM Interfaces Using the Vibrational Stark Effect. *J. Phys. Chem. C* **2017**, *121*, 22274−22285.

(25) Schkolnik, G.; Salewski, J.; Millo, D.; Zebger, I.; Franzen, S.; Hildebrandt, P. Vibrational Stark Effect of the Electric-Field Reporter 4-mercaptobenzonitrile as a Tool for Investigating Electrostatics at Electrode/SAM/Solution Interfaces. *Int. J. Mol. Sci.* **2012**, *13*, 7466−82.

(26) Andrews, S. S.; Boxer, S. G. Vibrational Stark Effects of Nitriles II. Physical Origins of Stark Effects From Experiment to Perturbation Models. *J. Phys. Chem. A* **2002**, *106*, 469−477.

(27) Andrews, S. S.; Boxer, S. G. Vibrational Stark Effects of Nitriles I. Methods and Experimental Results. *J. Phys. Chem. A* **2000**, *104*, 11853−11863.

(28) Fica-Contreras, S. M.; Daniels, R.; Yassin, O.; Hoffman, D. J.; Pan, J.; Sotzing, G.; Fayer, M. D. Long Vibrational Lifetime R-Selenocyanate Probes for Ultrafast Infrared Spectroscopy: Properties and Synthesis. *J. Phys. Chem. B* **2021**, *125*, 8907−8918.

(29) Saggu, M.; Levinson, N. M.; Boxer, S. G. Experimental Quantification of Electrostatics in X-H···pi Hydrogen Bonds. *J. Am. Chem. Soc.* **2012**, *134*, 18986−97.

(30) Blasiak, B.; Ritchie, A. W.; Webb, L. J.; Cho, M. Vibrational Solvatochromism of Nitrile Infrared Probes: Beyond the Vibrational Stark Dipole Approach. *Phys. Chem. Chem. Phys.* **2016**, *18*, 18094−111.

(31) Baiz, C. R.; Blasiak, B.; Bredenbeck, J.; Cho, M.; Choi, J. H.; Corcelli, S. A.; Dijkstra, A. G.; Feng, C. J.; Garrett-Roe, S.; Ge, N. H.; et al. Vibrational Spectroscopic Map, Vibrational Spectroscopy, and Intermolecular Interaction. *Chem. Rev.* **2020**, *120*, 7152−7218.

(32) Onsager, L. Electric Moments of Molecular Liquids. *J. Am. Chem. Soc.* **1936**, *58*, 1486−1493.

(33) Yan, C.; Thomaz, J. E.; Wang, Y. L.; Nishida, J.; Yuan, R.; Breen, J. P.; Fayer, M. D. Ultrafast to Ultraslow Dynamics of a Langmuir Monolayer at the Air/Water Interface Observed With Reflection Enhanced 2D IR Spectroscopy. *J. Am. Chem. Soc.* **2017**, *139*, 16518−16527.

(34) Karthick Kumar, S. K.; Tamimi, A.; Fayer, M. D. Comparisons of 2D IR Measured Spectral Diffusion in Rotating Frames Using Pulse Shaping and in the Stationary Frame Using the Standard Method. *J. Chem. Phys.* **2012**, *137*, 184201.

https://doi.org/10.1021/acs.jpcb.2c06071
J. Phys. Chem. B 2023, 127, 717−731

(35) Hoffman, D. J.; Fica-Contreras, S. M.; Pan, J.; Fayer, M. D. Pulse-Shaped Chopping: Eliminating and Characterizing Heat Effects in Ultrafast Infrared Spectroscopy. *J. Chem. Phys.* **2020**, *153*, 204201.
(36) Heverly-Coulson, G. S.; Boyd, R. J. Systematic Study of the Performance of Density Functional Theory Methods for Prediction of Energies and Geometries of Organoselenium Compounds. *J. Phys. Chem. A* **2011**, *115*, 4827−31.
(37) Hickey, A. L.; Rowley, C. N. Benchmarking Quantum Chemical Methods for the Calculation of Molecular Dipole Moments and Polarizabilities. *J. Phys. Chem. A* **2014**, *118*, 3678−87.
(38) Clabo, D.A.; Allen, W. D.; Remington, R. B.; Yamaguchi, Y.; Schaefer, H. F. A Systematic Study of Molecular Vibrational Anharmonicity and Vibration-Rotation Interaction by Self-Consistent-Field Higher-Derivative Methods. Asymmetric Top Molecules. *Chem. Phys.* **1988**, *123*, 187−239.
(39) Barone, V. Anharmonic Vibrational Properties by a Fully Automated Second-Order Perturbative Approach. *J. Chem. Phys.* **2005**, *122*, 14108.
(40) Tokmakoff, A. Orientational Correlation Functions and Polarization Selectivity for Nonlinear Spectroscopy of Isotropic Media. I. Third Order. *J. Chem. Phys.* **1996**, *105*, 1−12.
(41) Tan, H.-S.; Piletic, I. R.; Fayer, M. D. Polarization Selective Spectroscopy Experiments: Methodology and Pitfalls. *J. Opt. Soc. Am. B* **2005**, *22*, 2009−2017.
(42) Bian, H.; Zhao, W.; Zheng, J. Intermolecular Vibrational Energy Exchange Directly Probed with Ultrafast Two Dimensional Infrared Spectroscopy. *J. Chem. Phys.* **2009**, *131*, 124501.
(43) Hoffman, D. J.; Fica-Contreras, S. M.; Fayer, M. D. Amorphous Polymer Dynamics and Free Volume Element Size Distributions From Ultrafast IR Spectroscopy. *Proc. Natl. Acad. Sci. U.S.A.* **2020**, *117*, 13949−13958.
(44) Zhao, R.; Shirley, J. C.; Lee, E.; Grofe, A.; Li, H.; Baiz, C. R.; Gao, J. Origin of Thiocyanate Spectral Shifts in Water and Organic Solvents. *J. Chem. Phys.* **2022**, *156*, 104106.
(45) Brewer, S. H.; Franzen, S. A Quantitative Theory and Computational Approach for the Vibrational Stark Effect. *J. Chem. Phys.* **2003**, *119*, 851.
(46) Schneider, S. H.; Kratochvil, H. T.; Zanni, M. T.; Boxer, S. G. Solvent-Independent Anharmonicity for Carbonyl Oscillators. *J. Phys. Chem. B* **2017**, *121*, 2331−2338.

https://doi.org/10.1021/acs.jpcb.2c06071
J. Phys. Chem. B 2023, 127, 717−731